ADVANCED ENGINEERING MATERIALS
www.aem-journal.com

On the Mechanism of Formation of Bimodal Grain Structure in Al–4.5Mg–0.7Sc–0.3Zr Alloy Processed by Laser Powder Bed Fusion

*Polina Chernyshova, Teresa Guraya, Ana Martinez-Amesti, Hegoi Andonegi, Sarat Singamneni, and Zhan Wen Chen**

Scalmalloy is an Al–Mg alloy with additions of Sc and Zr originally developed as a high-strength aluminum alloy with $\sigma_{0.2} \geq 450$ MPa for aerospace industry. It is now well understood that the alloy is amendable for processing by laser powder bed fusion (LPBF). However, the mechanism of formation of the equiaxed-columnar bimodal grain structure during LPBF is not ascertained yet, fully. Herein, this gap is addressed with special focus on the distributions of critical elements such as Sc and various particles that form during LBPF. It is found that strong and weak segregation of Mg and Sc, respectively, occurs in the final solidification areas of the fine- and equiaxed-grain regions. The coarser and columnar grain regions show weak segregation of Mg and no Sc segregation. A priori knowledge on the Al–Sc eutectic reaction, its dependence on cooling rates, and the well-known thermal and solidification conditions related to the track location during LPBF is used to ascertain the mechanism of formation of the bimodal grain structure. The mechanism suggested is substantiated by the location-dependent elemental distributions and the various particles that are observed.

1. Introduction

Along with the laser powder bed fusion (LPBF)-additive manufacturing (known also as 3D printing) gradually becoming more widely applied in the last few years, LPBF of aluminum alloys has been intensively studied.[1] Research has shown that, through alloy modification or mixing additives in the alloy powder, the high-strength 2xxx and 7xxx aluminum alloys can be processed by LPBF.[1,2] However, LPBF of parts or structures using 2xxx and 7xxx alloys is yet to be reported for safety-critical loading applications. Scalmalloy is a high-strength aluminum alloy that has been specially developed for aerospace applications and proven suitable for processing by LPBF.[2] As was explained by Schmidtke et al.,[3] the alloy development was based on using an Al–4.5Mg (5xxx) alloy with small additions of Sc (0.66 wt%) and Zr (0.37 wt%). The additions have allowed for the alloy to be age hardenable with yield strength (σ_y) reaching ≈500 MPa in peak-hardening condition and for the alloy to be highly printable without hot cracking. However, the mechanism of forming the microstructures free of hot cracking during LPBF is yet to be understood fully.

Following the work by Schmidtke et al., a series of studies were undertaken by Spierings et al.,[4–8] further demonstrating the equiaxed-columnar bimodal structures within each track and the possibilities to attain high strengths after one-step aging. They observed Al_3(Sc,Zr) nanoparticles 30–100 nm in size and Al–Mg-oxides under the condition of low scan speed (=351 mm s^{-1}) using laser power (P) of 200 W (thus $P/v = 0.57$ J mm^{-1}). They assumed that these particles act as nuclei for forming the equiaxed grains next to the track boundary.[5] The original source of Al_3(Sc,Zr) nanoparticles, however, is less clear. Beyond the melt zone that solidifies into equiaxed grains and more inside the melt track, they suggest that

P. Chernyshova, S. Singamneni, Z. W. Chen
Department of Mechanical Engineering
Auckland University of Technology
Auckland 1010, New Zeland
E-mail: zhan.chen@aut.ac.nz

T. Guraya
Department of Mining & Metallurgical Engineering & Materials Science
University of the Basque Country
UPV/EHU
Bilbao 48013, Spain

A. Martinez-Amesti
SGIker
Advanced Research Facilities
University of the Basque Country
UPV/EHU
Donostia-San Sebastian 20018, Spain

H. Andonegi
AZTERLAN
Basque Research and Technology Alliance (BRTA)
Durango 48200, Spain

The ORCID identification number(s) for the author(s) of this article can be found under https://doi.org/10.1002/adem.202300135.

DOI: 10.1002/adem.202300135

Al_3(Sc,Zr) particles melt due to higher melt temperatures as predicted by their simulation. As a result, columnar grain growth occurs during solidification. Thus, in effect, they have suggested that Al_3(Sc,Zr) particles having survived in the melt region next to track boundary that later solidifies in equiaxed-grain solidification mode have come from the remelting of the previous track/layer. This mechanism of remelting of the previous layer leaving Al_3(Sc,Zr) particles unmelted in the region next to track boundary was soon more firmly proposed by Yang et al.[9]

As Spierings et al.[5] have explained, Al_3(Sc,Zr) nanoparticles acting as nuclei for the formation of equiaxed grains during LPBF is reasonable as Al_3(Sc,Zr) particles nucleating α-Al equiaxed grains during conventional casting has been well known. However, equiaxed-grain formation during casting does not need preexisting Al_3(Sc,Zr) particles. Hyde et al.[10] demonstrated the grain-refining effect of Al_3Sc during solidification of the Al–0.7wt%Sc alloy which was first melted and held at 750 °C. This melt temperature is above the liquidus temperature of the alloy meaning that Al_3Sc particles are not present in the melt and Al_3Sc nuclei form first from the melt upon cooling and at the start of solidification for the subsequent equiaxed α-Al-grain growth. Thus, it is unclear why Al_3(Sc, Zr) nuclei need to come from the melting of the previous layer/track so as to form equiaxed grains during LPBF.

Since Spierings et al.'s studies, there has continuously been a strong research effort on a number of aspects of LPBF of Al–Mg alloys containing various amounts of Sc and/or Zr.[11–23] Contents of Sc and Zr differ in various studies so that the kinetics of forming Al_3(Sc,Zr) may differ. In Zhang et al.'s[11] study using $P/v = 0.18\ \mathrm{J\,mm^{-1}}$, Al_3(Sc,Zr) particles up to 90 nm are found in the as-built state. In Shi et al.'s[12] study using P/v from 0.07 to $0.62\ \mathrm{J\,mm^{-1}}$, in contrast, there are no Al_3(Sc,Zr) particles that can be detected in their scanning transmission electron microscope (STEM) analysis. Churyumov et al.[13] also could not detect Al_3(Sc,Zr) particles in transmission electron microscope (TEM) analysis of their (P/v=) $0.81\ \mathrm{J\,mm^{-1}}$ samples. In Ma et al.'s[14] work using $P/v = 0.27\ \mathrm{J\,mm^{-1}}$, no Al_3(Sc,Zr) particles could be detected.

However, the suggestion of the mechanism relating to remelting seems to be still prevailing as described in a recent review on the progress of aluminum-alloy LPBF[24] and in a review specifically on LPBF of Sc-containing aluminum alloys.[25] Recently, Ekubaru et al.[23] demonstrated that controlling hatch spacing can control the amount of equiaxed grains and thus can control the strength of the alloy through grain-boundary strengthening. A recent effort on the alloy design for microstructure control in LPBF of aluminum alloys also was centered on the modification of the alloys using Sc.[26] A more thorough understanding of the role of Sc in forming the bimodal microstructure in Scalmalloy is thus important.

In this study, Scalmalloy samples have been made using a suitable set of LPBF process conditions. Equiaxed and columnar grain regions have been accurately sampled in specimens and analyzed to improve the understanding of how the elements, particularly Sc, redistribute during solidification. Further, the role of Sc in controlling the solidification modes and the consequent formation of the bimodal grain structure is explored. The common knowledge on the process thermodynamics, thermal conditions, and the rates at which the solid–liquid fronts advance is used to evaluate the results and infer critical observations. The presence of Fe- and Mg–Si-rich particles along the grain boundaries and the interiors of grains in the regions next to and away the track boundaries respectively will be used to substantiate inferences drawn from the results.

2. Experimental Section

Samples of $6 \times 6 \times 10$ mm and $10 \times 10 \times 55$ mm in dimensions were built using a Renishaw AM400 Selective Laser Melting machine. Specific parameters were pulsed laser power $P = 370$ W, scan velocity $v = 1600\ \mathrm{mm\,s^{-1}}$, layer thickness of 30 μm, hatch spacing of 100 μm, meander hatching strategy of 67° rotation, and the base plate at room temperature. Considering pulsing laser, $P/v < 0.23\ \mathrm{J\,mm}$, which was low but is nowadays common, and was a suitable LPBF condition for lack of fusion free and for little keyhole pore formation. The chemical composition in wt% of the alloy powder, as specified in the test certificate of powder supplier (LPW), is presented in **Table 1**. For hardening treatment, samples were heated to and held at 325 °C in an electric heating furnace for up to 4 h and then air cooled. Tensile samples were machined from the built long samples to gauge length section 17.9 mm and diameter 5.05 mm and tensile testing was conducted using a Tinius Olsen H50KS tester. Microhardness measurement was conducted using a Leco Microhardness Tester (LM800AT) with a 300 g loading for 10 s.

For microstructure analysis, samples were first prepared following the normal metallographic procedure with the final polishing down to silica 50 nm. Samples were observed using a JEOL JSM 7000F field-emission-gun scanning electron microscope (FEG-SEM) with 5 kV operating voltage. Lamellae 50–70 nm in thickness were prepared in selected locations, via standard lift-out protocol using a Dual Beam Helios 650 model which consisted of a 30 kV field-emission scanning electron column with 0.9 nm resolution and a 30 kV Ga focused-ion beam. The location of a lamella could be taken in an equiaxed grain region, a columnar grain region, or an equiaxed-columnar boundary region. **Figure 1** is an example showing a lamella being taken out from a columnar grain region. The lamellae were analyzed using Talos F200i field-emission-gun transmission electron microscope (FEG–TEM) equipped with a Bruker X-Flash100 energy-dispersive X-ray spectroscopy (EDS) spectrometer. Elemental maps were performed by EDS in the STEM mode under high-angle annular dark-field (HAADF) detector for Z contrast imaging in STEM conditions with a camera length of 200 mm using a pixel size of 2 nm, a dwell time of 900 s, and an image size of 512×512 pixels. Moreover, EDS microanalyses were carried out using a probe current of 800 pA and a semi-convergence angle of 6 mrad. Velox software was used for the compositional map acquisition and processing.

Table 1. Composition of as-received Scalmalloy powder.

	Al	Mg	Sc	Zr	Mn	Fe	Si	O	Zn,Cu,Ti,V
wt%	Bal.	4.55	0.65	0.30	0.51	0.14	0.16	0.04	Each ≤0.02

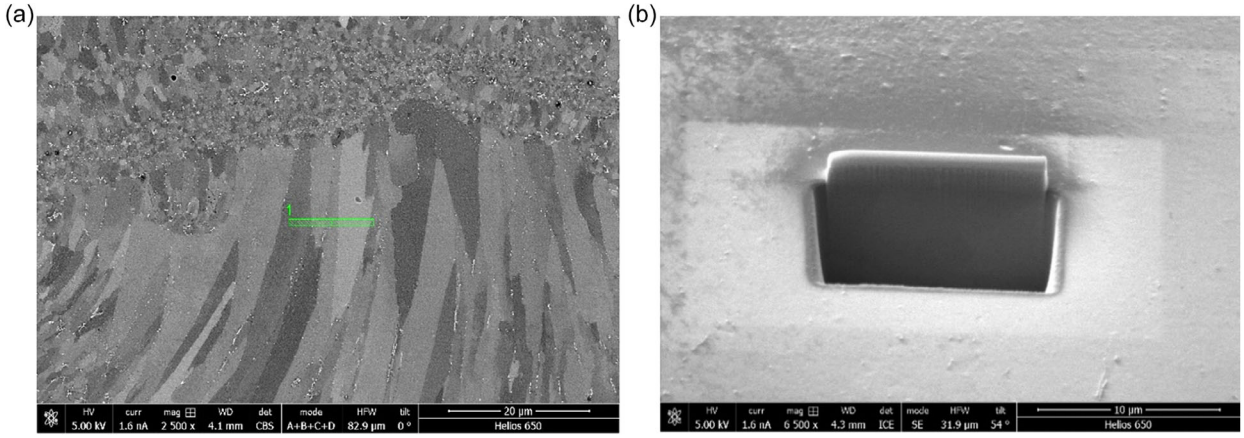

Figure 1. Illustration of a transmission electron microscope (TEM) lamellae being taken: a) field-emission-gun scanning electron microscope (FEG–SEM) micrograph showing an equiaxed-grain region on top of a columnar grain region with the lamella to be taken in the columnar grain region indicated by the green rectangular, and b) the material in the front part having been taken out by focused-ion beam with material behind to be further taken out to form a lamella.

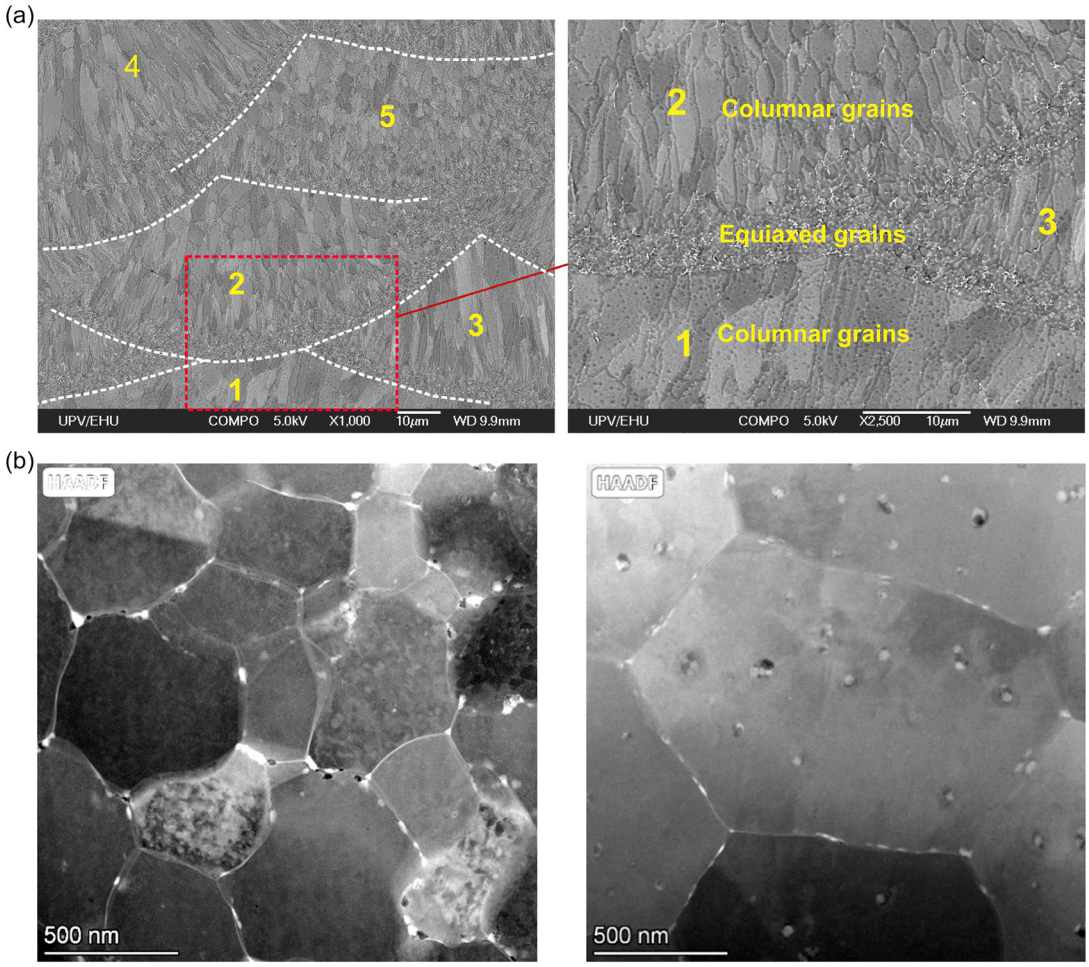

Figure 2. Bimodal grain structure in as-built state: a) FEG–SEM images showing equiaxed and columnar grains in each track with tracks 1–5 numbered and track boundaries outlined, and b) scanning transmission electron microscope (STEM) images of equiaxed grains adjacent to track boundary (left) and next/transitioning to columnar grain region (right).

3. Results and Discussion

3.1. Microstructures and Elemental Distribution in As-Built State

SEM micrographs are presented in **Figure 2** showing the typical microstructure in each track starting from fine-equiaxed grains a few microns in thickness next to and along the track boundary and then columnar grains inside the whole track. The grain size in the equiaxed-grain region next to track boundary is ≈0.5 μm and next to the columnar grain region is ≈1.5 μm, as shown by the STEM micrographs in Figure 2b. The grain width in columnar grain region is up to 3–4 μm (Figure 2a). The bimodal microstructures as evident in Figure 2 are typical with LPBF-processed Scalmalloy as already stated in the introduction. A distinctive feature observed in the present work in equiaxed grains is that there appear no particles inside the grains in the fine-grain region (left of Figure 2b) but particles can be seen inside each grain in the coarser and equiaxed grains next to the columnar grain region (right of Figure 2b).

The STEM image taken in the fine-equiaxed-grain (≈0.5 μm size) region next to track boundary is shown again in **Figure 3**, together with the corresponding EDS elemental (Al, Mg, Sc, Mn, Si, Zr, Fe, and O) maps. There are two major features in the image and the maps. The first is that no Sc/Zr-rich particles can be detected. Particles can be observed along the grain boundaries and these particles are rich in Mg and Si or in Fe possibly containing Mn but these particles are not Sc or Zr rich.

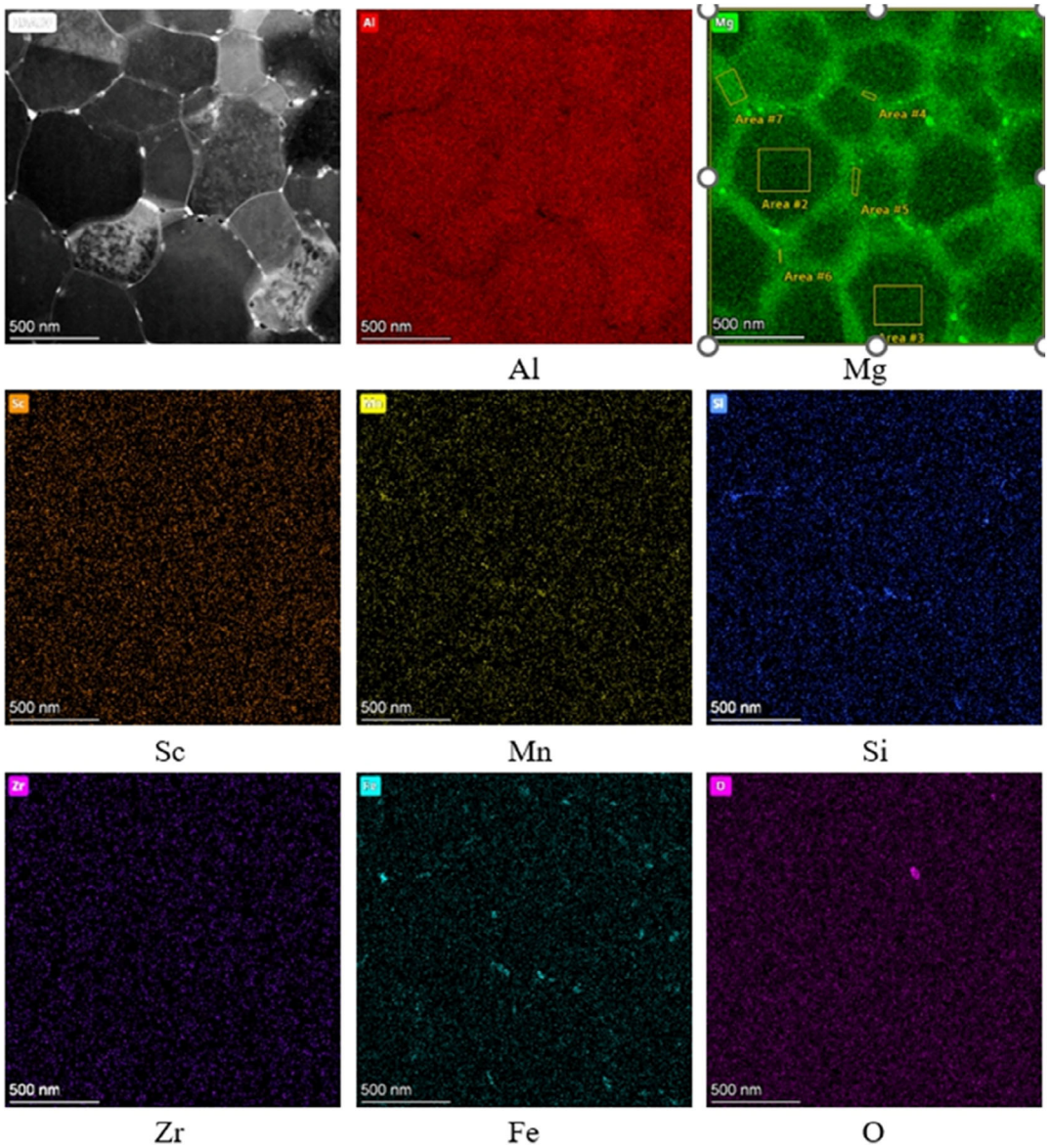

Figure 3. STEM high-angle annular dark-field (STEM–HAADF) micrograph, top left, and EDS elemental maps taken and analyzed in equiaxed-grain region adjacent to track boundary in an as-built sample. Small areas indicated as 2–7, with the whole area of the map being 1, indicate areas that were compositionally determined.

However, these particles are not observed away from the grain boundaries. Inside the grains, there are no particles (of a few to a few tens of nanometers in size), as has already been pointed out. As is shown in Table 1, Scalmalloy contains Fe and Si. Thus, Mg_2Si- and Fe-containing intermetallic particles form in the later stages of solidification and are present in the grain-boundary regions, as is commonly known in cast Al-alloy solidification.

The second feature in Figure 3 is the segregation of Mg along the grain boundaries, not just the very rich Mg-rich particles, as is clear in the Mg map. To further understand, area compositions inside the grains and in a number of other areas each including a section of a grain boundary have been evaluated. An EDS spectrum can include a small Cu and a small Ga peak as a Cu grid was used and the sample can be slightly contaminated by Ga during lamellae preparation. They have thus been excluded in ZAF calculation. For the present purpose of examining elemental distributions, only Al, Mg, and Sc are selected for ZAF calculation, since these are the primarily important elements of the alloys. Thus, the composition is viewed normalized. Note that, from Table 1, atom percentage of Zr is low and a content at 0.3 wt % (<0.1 at%) is difficult for EDS to accurately determine. Sc is the major element to form Al_3(Sc,Zr). **Table 2** lists the normalized compositions, corresponding to the areas marked in the Mg map in Figure 3. The (grain-boundary) areas selected for EDS analysis do not include any particles.

As listed in Table 2, the overall Mg content is 4.9 wt% in Area 1, which is the whole of the area in the STEM micrograph of Figure 3, while areas 2 and 3 representing the interior regions of the grains showed an average of 3.5 wt% Mg, which is significantly (30%) lesser, compared to the whole area. In contrast, the average Mg content at 6.6 wt% is typical of aaareas 4, 6, and 7, that are grain-boundary regions. This is around 34% higher Mg content compared to the whole region response. Thus, the EDS analytical data clearly demonstrates the Mg enrichment in grain-boundary areas, as is readily evidenced in the Mg map in Figure 3, where EDS analysis on Area 5 (Figure 3) shows a 4.8 wt% of Mg. The area is closer to the grain boundary but is also a combination of areas at the grain boundary and the interior.

Table 2. Normalized wt% of Al, Mg, and Sc determined by STEM–EDS in area shown and each number in subscript indicates the area number stated in the Mg map in Figure 3.

Areas indicated in Figure 3	Al	Mg	Sc
Whole$_1$	**94.49**	**4.93**	**0.58**
Grain inside$_2$	96.06	3.42	0.52
Grain inside$_3$	95.93	3.51	0.56
Grain inside average	**95.99**	**3.47**	**0.54**
Grain boundary$_4$	93.07	6.06	0.87
Grain boundary$_5$	94.61	4.78	0.60
Grain boundary$_6$	92.27	6.76	0.96
Grain boundary$_7$	92.34	7.04	0.62
Grain boundary mean	**93.07**	**6.16**	**0.77**
Grain boundary standard deviation (SD)	1.09	1.01	0.18
Grain boundary standard error	0.54	0.50	0.09

The overall Sc content is low due to the initial Sc content being only 0.65 wt% and the peak in an EDS spectrum is clear but not very strong leading to EDS determination less certain in this low wt%. However, values of Sc content listed in Table 2 may suggest possibly a slight segregation of the element to grain boundary, although there is no indication of Sc enrichment in the Sc map (Figure 3). The overall Sc content determined is 0.58 wt% (area 1 in Table 2), although Sc in the original powder is slightly higher. Areas 2 and 3 are grain interiors and their Sc contents at 0.52–0.56 wt% may be viewed slightly lower (3–10%) than the overall Sc content. Areas 4, 6, and 7 are primarily grain-boundary areas and their Sc contents are 0.87, 0.96, and 0.62 wt%, respectively. Thus, on average, Sc content in grain-boundary areas detected can generally be viewed from slightly (7%) higher to considerably (65%) higher than the overall Sc content (0.58 wt%), although the accuracy for the low-concentration detection may not be very high. Thus, Sc may also have redistributed and segregated at least slightly to grain boundaries during LPBF-equiaxed-grain solidification of the alloy, although more evidence is required to confirm if a weak segregation of Sc to the gain boundaries has occurred.

Away from the equiaxed-grain region, the features shown in the STEM image and EDS elemental maps in **Figure 4** are very different for the columnar grain region and almost opposite to those observed in the equiaxed-grain region. First, particles that appear to be Mg–Si rich and Fe rich are mostly observed inside the grains as against being frequently at the grain boundaries. As has been pointed out, referring to Figure 2b, right, in the coarser grain side of the equiaxed-grain region bridging to columnar grain region, particles are also present inside the grains. Again, as indicated by the Sc and Zr maps in Figure 4, there is no detectable presence of Sc- or Zr-rich particles. Second, the Mg map in Figure 4 has suggested only a weak enrichment of Mg in the grain-boundary areas of the columnar grain region, very different from the strong grain-boundary Mg enrichment in equiaxed-grain region shown in the Mg map in Figure 3.

Similar to providing the normalized compositions for equiaxed grains as explained before, **Table 3** lists the compositions corresponding to the areas marked in the STEM micrograph in Figure 4. The overall composition (Area 1) in Table 3 is very close to the alloy composition listed in Table 1. About 10%Mg, =(4.55–4.12)/4.55, has been depleted inside the grains and segregated at the grain boundaries of the columnar grains. This is a weak segregation, in comparison to ≈24%Mg, =(4.55–3.47)/4.55, that has segregated in the grain-boundary areas in the equiaxed-grain region. There appears no segregation of Sc that can be detected according to the data of Sc content values shown in Table 3 for the columnar grain region. This compares to the weak Sc segregation to grain boundaries in the fine-equiaxed-grain region shown in Table 2, as discussed before.

3.2. LPBF and Solidification Path

Referring to the Al–Mg-phase diagram, the slopes of the liquidus and solidus are both negative meaning that, as Mg content increases, liquidus and solidus temperatures decrease (till ≈18 wt%). Thus, for a 4.5 wt%Mg–Al alloy, Mg rejection during solidification and enrichment in the final solidification location

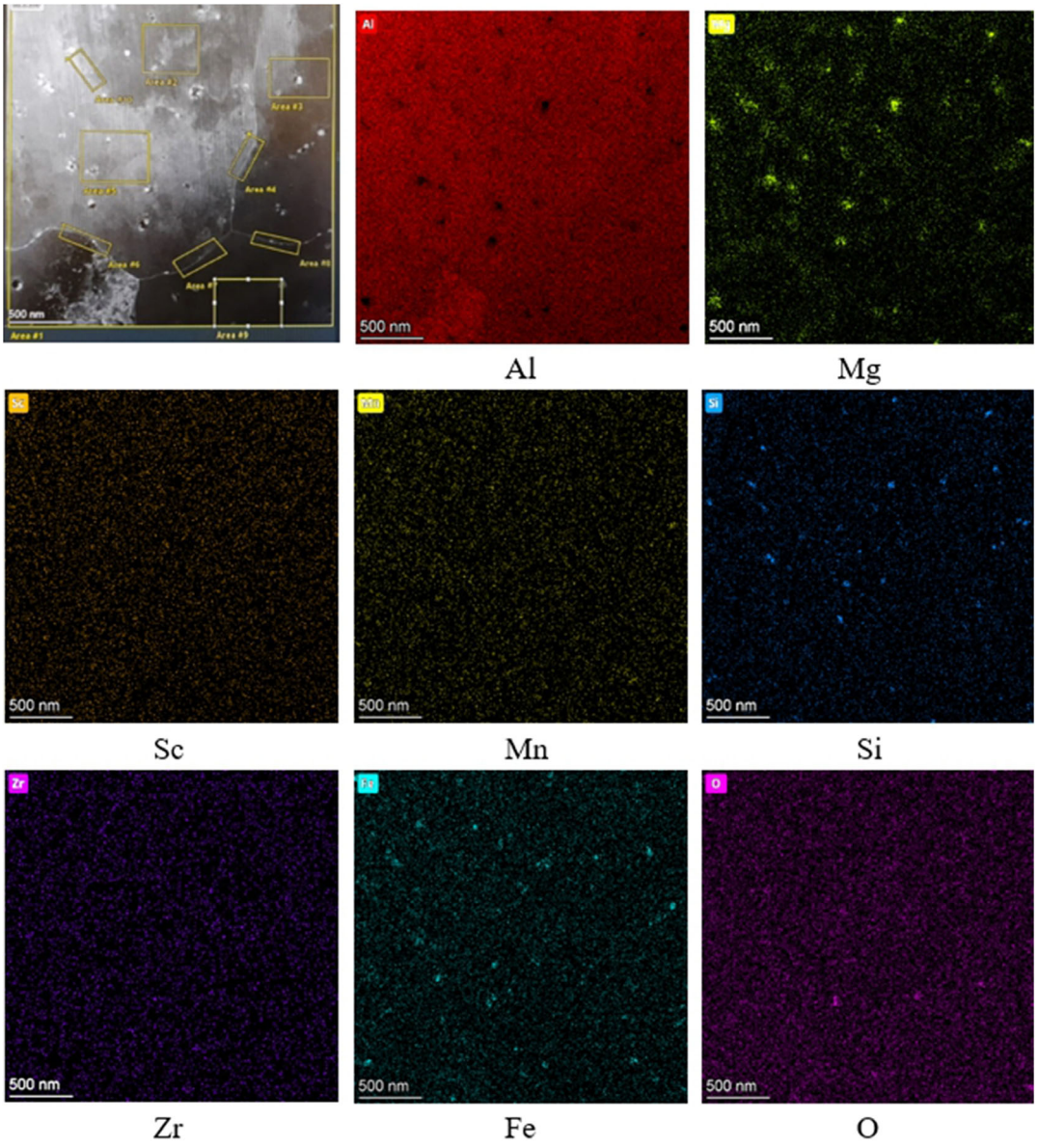

Figure 4. STEM–HAADF micrograph, top left, and EDS elemental maps taken and analyzed in columnar grain region ≈50 μm from track boundary in an as-built sample. Small areas indicated as 2–10, with the whole area of the map being 1, indicate areas that were compositionally determined.

Table 3. Normalized wt% of Al, Mg, and Sc determined by STEM–EDS in areas shown in the top left map in Figure 4.

	Area 1 **Whole**	Area 2 Inside	Area 3 Inside	Area 4 GB	Area 5 Inside	Area 6 GB	Area 7 GB	Area 8 GB	Area 9 Inside	Area 10 GB	**Inside mean** & SD	**GB mean** & SD
Al	**94.78**	94.98	95.04	94.89	94.94	93.75	95.27	94.07	95.49	93.33	**95.11** ± 0.25	**94.50** ± 0.71
Mg	**4.53**	4.25	4.25	4.44	4.42	5.54	4.10	5.16	3.69	5.85	**4.15** ± 0.32	**4.81** ± 0.66
Sc	**0.69**	0.77	0.71	0.67	0.66	0.71	0.63	0.78	0.83	0.82	**0.74** ± 0.07	**0.70** ± 0.06

meaning a segregation to grain boundaries is expected if solid–liquid front growth velocity (R) is sufficiently low to allow for sufficient diffusion. As is explained by Kurz and Trivedi,[26] when R reaches 0.8 m s^{-1} or is higher, solute trapping occurs during rapid solidification. Solute trapping should mean segregation free. During LPBF, solidification in a melt track starts at track boundary with $R = 0$. This is because the angle (θ) between the solidification front moving direction and scan direction is 90°. Next to track boundary, R increases very rapidly as the distance from track boundary increases. Segregation in the region

next to track boundary is thus expected due to the very low R values. The presence of Mg–Si- and Fe-containing particles only in grain-boundary areas in the fine-equiaxed-grain region can also be expected to be the result of segregation of these elements during solidification due to the very low R.

During laser processing, as in laser welding and LPBF, θ decreases and R increases rapidly away from track boundary.[27] The exact shape of the melt pool during LPBF is not clear. Del Guercio et al.,[28] in treating diffusion and segregation during LPBF of an Al alloy, take $\theta = 45°$. For this θ value and for $v = 1600$ mm s^{-1} in our case, $R = 1600\,\text{mm s}^{-1} \times \cos 45° = 1.1\,\text{m s}^{-1}$. At this R value, solute trapping during solidification occurs. However, $\theta = 45°$ means a short melt pool during LPBF, as the length is comparable to the depth of the melt pool. A length/depth ratio of 2 and 3 would mean $\theta = 63.4°$ and $\theta = 71.6°$, then, $R = 0.7$ and $0.5\,\text{m s}^{-1}$, respectively. These R values are within the range of localization of diffusion but close to the critical R value for solute trapping.[27] Thus, only very low Mg segregation to grain boundary that has been observed in columnar grain region is reasonable. This is also consistent with the Mg_2Si- and Fe-containing particles observed mainly in grain interiors in the coarser equiaxed-grains and in the whole columnar grain region, as the high R values also prevent Si and Fe to diffuse to grain boundaries to form particles there during solidification.

The slight segregation of Sc to grain boundaries in the equiaxed-grain region but not in columnar grain region, however, may need to consider further. Al–Sc-phase diagram suggests that, for the alloy containing 0.65 wt%Sc, eutectic should form after the formation of pro-eutectic Al_3Sc during cooling. The pro-eutectic Al_3Sc or $Al_3(Sc,Zr)$ should act as nuclei whether they can be detected or not. However, the STEM image in Figure 3 does not display the normal coupled eutectic growth morphology. This is the result of a divorced eutectic solidification. Norman et al.[28] illustrate that, using an Al–0.7(wt%)Sc alloy and cooling rate up to 1000 K s^{-1}, no evidence of couple growth could be found under TEM investigation. They show that only α(Al) grows outward from the Al_3Sc nucleus, typical of a divorced eutectic growth. This growth then should result in a small amount of Sc being rejected during the growth. Thus, segregating for a short distance to grain-boundary areas should result as, in the fine-equiaxed-grain-boundary region, the growth rate is low and diffusion is allowed.

Moving away from track boundary, R and cooling rate (dT/dt) increase very rapidly.[27] An increase in dT/dt may have a strong effect on the effectiveness of Sc to form and thus to grain refine. To illustrate, we discuss using the Al–Sc binary system. The equilibrium Al–Al_3Sc eutectic composition is 0.56 wt%,[2,29] and thus the formation of pro-eutectic Al_3Sc in the present Scalmalloy containing 0.65 wt%Sc is efficient to nucleate α(Al) in near-equilibrium solidification condition of the low R value region. However, under the rapid solidification and thus far from equilibrium condition in the melt away from track boundary, the effectiveness of Sc to form Al_3Sc and to grain refine can diminish. It has been demonstrated[29] that the values of eutectic composition are ≈0.6, ≈0.8, ≈1.3, and ≈3.0 wt% for dT/dt equal to 5, 10^2, 10^3, and 10^5 K s^{-1}, respectively. These data of nonequilibrium eutectic composition suggest that Sc in an Al–0.65 wt%Sc alloy would not be effective for grain refining if $dT/dt > 10^2$ K s^{-1}.

During LPBF, dT/dt increases sharply away from track boundary to very high values. Hooper[30] directly measured dT/dt of track surface during LPBF of Ti6Al4V to be $(1–40) \times 10^6$ K s^{-1} depending on LPBF parameters used. Hyer et al.[31] estimated dT/dt values of AlSi10Mg LPBF, based on the relationship between dT/dt and secondary arm spacing and on using the Rosenthal equation, to be 10^5–10^7 K s^{-1}. Thus, it is expected that dT/dt could reach at least 10^5 K s^{-1} a short distance away from track boundary. For the present alloy of 0.65 wt%Sc, although the alloy also contains 0.3 wt%Zr (0.09at%Zr), forming pro-eutectic Al_3Sc for grain refining during solidification may thus not be expected in most part of the melt. This effectiveness of grain refining depending on dT/dt may explain why increasing base plate temperature (T_B) increases the thickness of the equiaxed-grain region, as observed for example in Yang et al.'s study.[9] The increase in T_B should reduce the rate of heat transfer from the melt track, thus reduces dT/dt, assisting pro-eutectic Al_3Sc formation and thus widening the equiaxed-grain region.

3.3. Elemental Distribution after Aging Treatment

Figure 5 shows hardness values and tensile curves of samples in the as-built and in the one-step aged conditions. The results are for confirming the aging treatment used in this study to be in agreement with the data and heat-treatment conditions presented in the literature. As explained in Introduction section, one-step aging treatment for the alloy to achieve mid to high strength has been well understood. Further illustration of Sc distribution after aging treatment is not for the study of how Sc has played the role on precipitation strengthening. Rather, how aging treatment has affected the elemental distributions in the LPBF samples of the alloy presented here is for the further support of the understanding of the distributions in the as-built state. Thus, the suggested mechanism of how Sc affects the bimodal microstructure formed can be better understood.

The elemental distributions in the equiaxed-grain region of an aged sample are shown in **Figure 6**. The Mg map in Figure 6 shows that Mg content should be still higher in grain-boundary areas than the content in grain interiors. But Mg appears to be significantly less enriched in gran-boundary areas in Figure 6, in comparison to the high degree of enrichment in the areas shown in the Mg map in Figure 3. This is because a portion of Mg from the Mg-rich grain-boundary areas has diffused to grain interiors when the sample was held at the aging temperature. The Si map shown in Figure 6 displays an even distribution of Si, meaning that Mg–Si (likely Mg_2Si) particles that can be detected in the as-built state in Figure 3 have dissolved during aging treatment. The Fe map in Figure 6, compared to that in Figure 3, also has suggested that the Fe-rich particles in the as-built state have largely dissolved during aging treatment.

However, the Sc map shown in Figure 6 suggests the presence of Sc-rich particles after aging treatment, as opposite to the as-built state showing no Sc-rich particles in Figure 3. As has been explained, according to the literature, the strengthening Al_3Sc precipitates after aging treatment can be 1–2 nm or less in size. These small-size precipitates are not distinguishable in the Sc map of Figure 6. The Sc map in Figure 6 has suggested that there are Sc-rich particles larger than a few nanometers. Observing

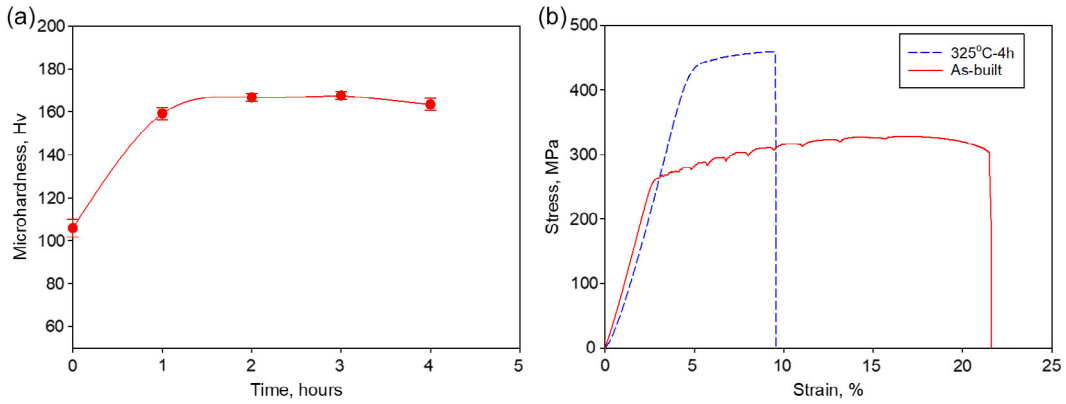

Figure 5. Mechanical testing: a) hardness values of samples heat-treated in various conditions, and b) selective tensile curves for one as-built and one aged samples.

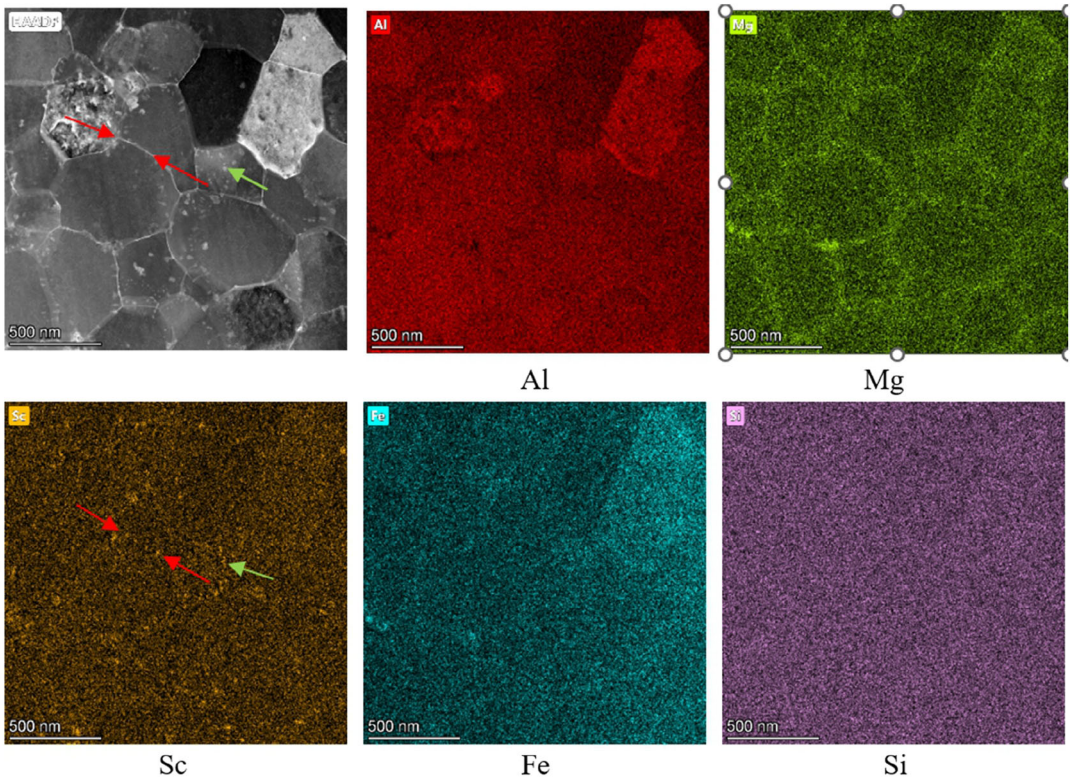

Figure 6. STEM–HAADF micrograph and elemental maps in equiaxed-grain region of a sample after aging treatment. Red arrows point to a section of a grain boundary in the STEM image and to Sc-rich particles along the same section in the Sc map. Green arrows points to a Sr-rich particle inside the grains.

closely the STEM micrograph and the Sc map in Figure 6 suggests that more Sc-rich particles are present along the grain boundaries. An example of such particles is pointed to by the two red arrows in Figure 6 in the STEM image and in the Sc map. Forming Sc-rich particles in grain-boundary areas during aging treatment is reasonable, as there is a slight Sc segregation to the areas during solidification in the equiaxed-grain region, as has already been shown and explained. Note also that Sc-rich particles are also observed in grain interiors and an example is indicated by a green arrow in both the STEM image and the map in Figure 6. Sc-rich particles larger than a few nanometers in size in grain interiors suggest that Sc supersaturation during solidification may not be homogeneous.

The elemental distributions in the columnar grain region of the aged sample are shown in **Figure 7**. Little Mg enrichment in the grain-boundary areas is shown in the Mg map. This is because the readily homogenization of Mg during aging treatment from the low Mg segregation in grain-boundary areas in the columnar grain region in the as-built state (as shown in Figure 4). Many Mg_2Si- and Fe-rich particles inside the grains

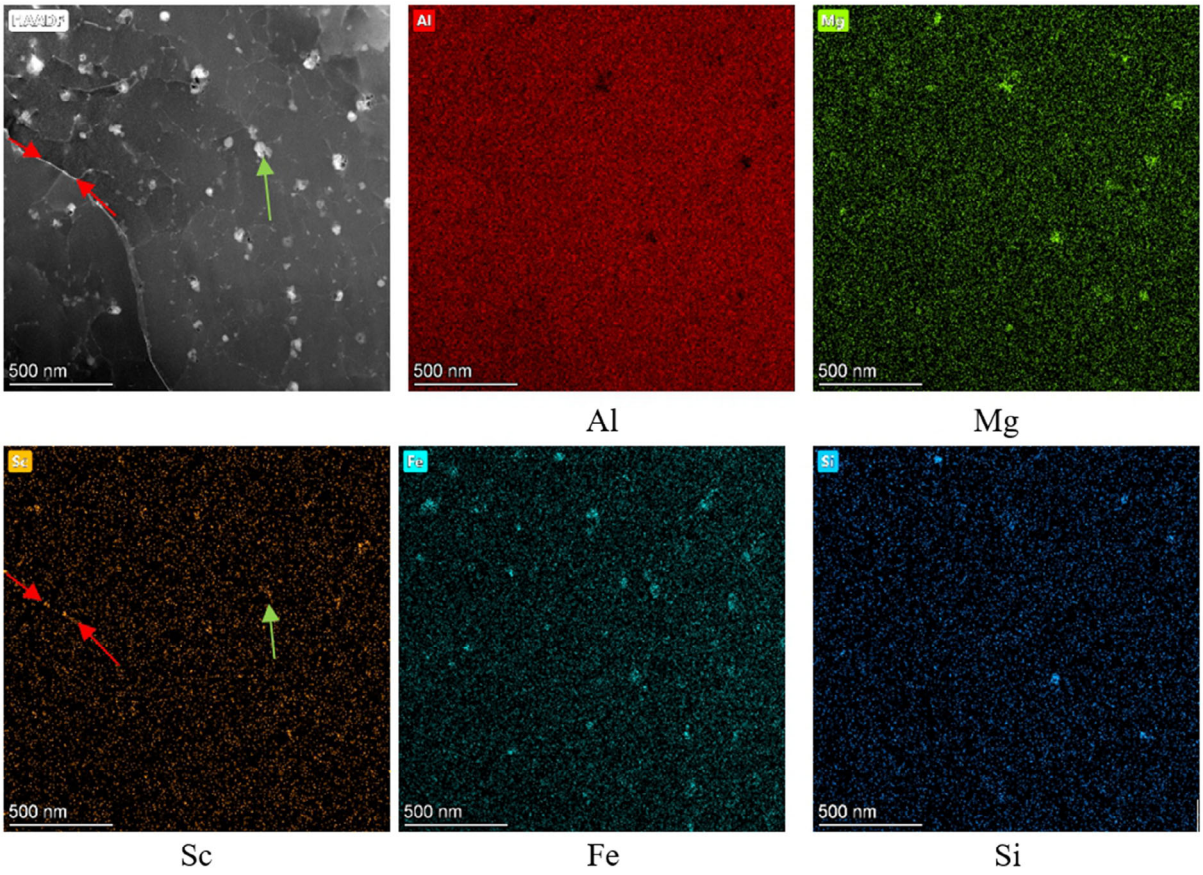

Figure 7. STEM–HAADF micrograph and elemental maps in columnar grain region of a sample after aging treatment. Red arrows point to a section of a grain boundary in the STEM image and to Sc-rich particles along the same section in the Sc map. Green arrows points to a Sr-rich particle inside the grains.

in the as-built state have however remained, as is indicated by the Mg, Si, and Fe maps in Figure 7. This is very different from the dissolution of the Mg–Si- and Fe-rich particles in grain boundaries in the as-built state during aging treatment and may be the result of rapid diffusion in the fine-equiaxed-grain region. Grain-boundary diffusion rate may be much higher than lattice diffusion rate and grain-boundary areas are large in the fine-equiaxed-grain region. Furthermore, in the fine-grain region, elemental diffusion only needs a short distance for elemental homogenization in grain interiors. In contrast, dissolution of particles most in grain interiors in the coarser and columnar grain region requiring lattice diffusion could be a much slower process. This may explain the insignificant amount of dissolution in the coarse and columnar grain region during the time at aging temperature. As for Sc, the Sc map in Figure 7 shows some Sc-rich particles throughout in this aged sample. This is consistent with the lack of Sc segregation to grain-boundary areas in columnar grain region in as-built state.

4. Conclusions

The LPBF-induced elemental distributions were found to be different in the solidification of equiaxed to columnar grain regions suggestively due to the conditions of solidification in LPBF. The very low growth and cooling rates in the region next to the track boundary allow for Al_3Sc to form and act as a nucleus for the fine-equiaxed-grain (≈0.5 μm) growth next to and along the track boundary. The very low growth rate also allows for elements to diffuse outward during solidification, as observed with segregation of elements to grain boundaries in the fine-equiaxed-grain region. The equiaxed-grain size increases to ≈1.5 μm over a few microns distance from track boundary as a result of the steep increase in the cooling rate away from track boundary. This results in the shifting of the composition of the divorced eutectic to higher values than the Sc content of the alloy. Thus, grain-refining effect diminishes and grain size increases. Further (only a few microns) away, grain-refining effect of Sc (with its content of the alloy) will be totally lost, resulting in a columnar grain growth. Away from track boundary, the high growth rate during solidification in the columnar grain region results in highly localized diffusion, preventing significant segregation during solidification.

Acknowledgements

Open access publishing facilitated by Auckland University of Technology, as part of the Wiley - Auckland University of Technology agreement via the Council of Australian University Librarians.

Conflict of Interest

The authors declare no conflict of interest.

Data Availability Statement

The data that support the findings of this study are available from the corresponding author upon reasonable request.

Keywords

boundaries, cooling, diffusion, grains, segregation, solidification

Received: January 29, 2023
Revised: March 22, 2023
Published online:

[1] I. M. Kusoglu, B. Gökce, S. Barcikowski, *Addit. Manuf.* **2020**, *36*, 101489.
[2] P. A. Rometsch, Y. Zhu, X. Wu, A. Huang, *Mater. Des.* **2022**, *219*, 110779.
[3] K. Schmidtkea, F. Palm, A. Hawkins, C. Emmelmann, *Phys. Procedia* **2011**, *12*, 369.
[4] A. B. Spierings, K. Dawson, M. Voegtlin, F. Palm, P. J. Uggowitzer, *CIRP Ann. Manuf. Technol.* **2016**, *65*, 213.
[5] A. B. Spierings, K. Dawson, T. Heeling, P. J. Uggowitzer, R. Schäublin, F. Palm, K. Wegener, *Mater. Des.* **2017**, *115*, 52.
[6] A. B. Spierings, K. Dawson, K. Kern, F. Palm, K. Wegener, *Mater. Sci. Eng. A.* **2017**, *701*, 264.
[7] A. B. Spierings, K. Dawson, P. J. Uggowitzer, K. Wegener, *Mater. Des.* **2018**, *140*, 134.
[8] A. B. Spierings, K. Dawson, P. Dumitraschkewitz, S. Pogatscher, K. Wegener, *Addit. Manuf.* **2018**, *20*, 173.
[9] K. V. Yang, Y. Shi, F. Palm, X. Wu, P. Rometsch, *Scr. Mater.* **2018**, *145*, 113.
[10] K. B. Hyde, A. F. Norman, P. B. Prangnell, *Acta Mater.* **2001**, *49*, 1327.
[11] H. Zhang, D. Gu, J. Yang, D. Dai, T. Zhao, C. Hong, A. Gasser, R. Popraw, *Addit. Manuf.* **2018**, *23*, 1.
[12] Y. Shi, K. Yang, S. K. Kairy, F. Palm, X. Wu, P. A. Rometsch, *Mater. Sci. Eng. A* **2018**, *732*, 41.
[13] A. Y. Churyumov, A. V. Pozdniakov, A. S. Prosviryakov, I. S. Loginova, D. K. Daubarayte, D. K. Ryabov, V. A. Korolev, A. N. Solonin, M. D. Pavlov, S. V. Valchuk, *Mater. Res. Express* **2019**, *6*, 126595.
[14] R. Ma, C. Peng, Z. Cai, R. Wang, Z. Zhou, X. Li, X. Cao, *J. Alloys Compd.* **2020**, *815*, 152422.
[15] J. Zhao, X. Xue, B. Wang, T. Liu, L. Luo, Y. Wang, L. Wang, Y. Su, J. Guo, H. Fu, *Mater. Sci. Eng. A.* **2021**, *825*, 141889.
[16] C. N. Kuo, P. C. Peng, D. H. Liu, C. Y. Chao, *Metals* **2021**, *11*, 555.
[17] Z. Wang, X. Lin, N. Kang, Y. Hua, J. Chen, W. Huang, *Addit. Manuf.* **2020**, *34*, 101260.
[18] Z. Wang, X. Lin, N. Kang, J. Chen, H. Tan, Z. Feng, Z. Qin, H. Yang, W. Huang, *J. Mater. Sci. Technol.* **2021**, *95*, 40.
[19] Z. Wang, X. Lin, N. Kang, Y. Wang, X. Yu, H. Tan, H. Yang, W. Huang, *Scr. Mater.* **2021**, *203*, 114052.
[20] X. Li, Y. Liu, Z. Zhou, *Mater. Charact.* **2022**, *190*, 112068.
[21] Y. Zhu, Y. Zhao, B. Chen, *Mater. Sci. Eng., A* **2022**, *833*, 142516.
[22] L. Cabrera-Correa, *Mater. Charact.* **2023**, *196*, 112549.
[23] Y. Ekubaru, O. Gokcekaya, T. Ishimoto, K. Sato, K. Manabe, P. Wang, T. Nakano, *Mater. Des.* **2022**, *221*, 110976.
[24] Z. Xiao, W. Yu, H. Fu, Y. Deng, Y. Wu, H. Zheng, *Virtual Phys. Prototyping* **2022**, *18*, e2125880.
[25] D. Bayoumy, W. Kan, X. Wu, Y. Zhu, A. Huang, *J. Mater. Sci. Technol.* **2023**.
[26] D. Schimbäck, P. Mair, M. Bärtl, F. Palm, G. Leichtfried, S. Mayer, P. J. Uggowitzer, S. Pogatscher, *Scr. Mater.* **2022**, *207*, 114277.
[27] W. Kurz, R. Trivedi, *Mater. Sci. Eng. A.* **1994**, *179–180*, 46.
[28] A. F. Norman, P. B. Prangnell, R. S. McEwen, *Acta Mater.* **1998**, *46*, 5715.
[29] L. S. Toropova, D. G. Eskin, M. L. Kharakterova, T. V. Dobatkina, *Advanced Aluminium Alloys Containing Scandium: Structure and Properties*, Taylor & Francis, Abingdon (UK), **1998**, p. 14.
[30] P. A. Hooper, *Addit. Manuf.* **2018**, *22*, 548.
[31] H. Hyer, L. Zhou, S. Park, G. Gottsfritz, G. Benson, B. Tolentino, B. McWilliams, K. Cho, Y. Sohn, *Metallogr., Microstruct., Anal.* **2020**, *9*, 484.